

How thick are Mercury’s polar water ice deposits?

Vincent R. Eke¹, David J. Lawrence², Luís F. A. Teodoro³

¹*Institute for Computational Cosmology, Department of Physics, Durham University, Science Laboratories, South Road, Durham DH1 3LE, U.K.*

²*Johns Hopkins University Applied Physics Laboratory, Laurel, MD 20723, U.S.A.*

³*BAER, Planetary Systems Branch, Space Science and Astrobiology Division, MS: 245-3, NASA Ames Research Center, Moffett Field, CA 94035-1000, U.S.A.*

17 November 2016

ABSTRACT

An estimate is made of the thickness of the radar-bright deposits in craters near to Mercury’s north pole. To construct an objective set of craters for this measurement, an automated crater finding algorithm is developed and applied to a digital elevation model based on data from the Mercury Laser Altimeter onboard the MESSENGER spacecraft. This produces a catalogue of 663 craters with diameters exceeding 4 km, northwards of latitude $+55^\circ$. A subset of 12 larger, well-sampled and fresh polar craters are selected to search for correlations between topography and radar same-sense backscatter cross-section. It is found that the typical excess height associated with the radar-bright regions within these fresh polar craters is (50 ± 35) m. This puts an approximate upper limit on the total polar water ice deposits on Mercury of $\sim 3 \times 10^{15}$ kg.

1 INTRODUCTION

The presence of water in the inner solar system is vital for the development of life. Violent collisions between planetary embryos are thought to have built the rocky planets (Morbidelli et al. 2012), and the associated high energies and temperatures would not have been conducive for volatile molecules such as water. The source of Earth’s water is therefore of considerable interest. Measurements of deuterium/hydrogen ratios of solar system bodies (Hartogh et al. 2011; Alexander et al. 2012) combined with models of accretion onto the Earth (Morbidelli et al. 2000; O’Brien et al. 2014) appear consistent with exogenous sources.

Both the Moon and Mercury provide relatively unweathered surfaces in comparison with the Earth, so their near-surface volatile inventories provide additional constraints on models of water delivery to the inner solar system. Surface volatiles are not stable for significant periods unless placed into the low temperature “cold traps” provided by near-polar impact craters containing permanently shaded regions. In order to discriminate between the various possible sources of water (Moses et al. 1999; Crider & Killen 2005), which often imply different amounts of water being delivered, one also needs to understand how efficiently it can migrate from the delivery location to the cold traps (Butler 1997; Ong et al. 2010; Stewart et al. 2011). Such models can then inform the interpretation of actual measurements of the volatile inventories of these bodies.

Various neutron spectroscopy, circularly polarized radar, albedo (IR, visible and UV) and impact measurements have been made of the Moon and Mercury to investigate their cold traps. While the LCROSS experiment (Colaprete et al. 2010) found a few per cent by mass of the material in Cabeus crater on the Moon was water ice, which is at a level consistent with neutron spectroscopy results (Eke et al. 2015), there is evidence for substantially purer water ice deposits near Mercury’s poles.

A remarkable increase in the same sense circular polarized radar backscatter cross-section was detected at wavelengths of 3.5 cm (Slade et al. 1992; Butler et al. 1993), 12.6 cm (Harmon & Slade 1992; Harmon et al. 1994, 2001) and 70 cm (Black et al. 2010) from Mercurian polar cold traps. One explanation for these radar returns

was that there was multiple scattering occurring within a low-loss medium such as water ice (Hapke 1990; Hagfors et al. 1997). The high radar backscatter regions correlated spatially with areas that have modelled surface or near-subsurface temperatures that remain below $\sim 100 - 150$ K (Paige et al. 1992; Ingersoll et al. 1992; Vasavada et al. 1999). This provided extra circumstantial evidence to motivate the interpretation of the anomalous radar measurements as indicating the presence of volatile molecules.

Instruments onboard the MESSENGER spacecraft (Solomon et al. 2007) have considerably increased the information available about the polar cold traps. The deficit in neutron flux observed over the poles is consistent with a localised hydrogen-rich layer extending down for tens of centimetres beneath a 10-20 cm thick layer that is less rich in hydrogen (Lawrence et al. 2013). These observations suggest that nearly pure water ice, and not an alternative volatile such as sulphur (Sprague et al. 1995), is responsible for the radar features. MESSENGER’s Mercury Dual Imaging System (MDIS) has allowed an improved determination of the locations of the permanently shaded regions, increasing the confidence with which they can be associated with the high radar backscatter regions (Chabot et al. 2012, 2013). Albedo measurements from the Mercury Laser Altimeter (MLA, Cavanaugh et al. 2007) at 1064 nm showed either bright or dark surfaces coincident with these polar cold traps (Neumann et al. 2013). The distinction matched temperature model predictions for either thermally stable water ice at the surface (high albedo) or under a ~ 10 cm thick organic lag deposit (low albedo) as noted by Paige et al. (2013).

More recently, the sensitivity of MDIS images has allowed the imaging of permanently shaded regions using scattered light (Chabot et al. 2014). The results are similar to the MLA albedo measurements, albeit at visible wavelengths, with anomalous reflectance regions largely coincident with radar-bright ones. Of the surveyed areas, only Prokofiev crater has a high albedo in MDIS images, with the other radar-bright regions appearing anomalously dark. The imaging in Prokofiev crater shows a ~ 3 km-wide zone that is still in permanent shade with high radar reflectivity, but lies outside the high MDIS reflectance area. One possible reason for this could be the presence of a stable subsurface ice deposit that

arXiv:1611.05395v1 [astro-ph.EP] 16 Nov 2016

does not affect the surface reflectance. Chabot et al. (2014) further note that the imaged, high-reflectance region displays a similar texture to that in the sunlit region of Prokofiev, suggesting a relatively recent ice deposition onto a previously cratered surface. Deutsch et al. (2016) used a combination of MLA-derived topography and MDIS imagery to show that radar-bright features collocate with regions of both permanent (from MLA) and persistent (from MDIS) shadow. Furthermore, they demonstrated that many regions of persistent or permanent shadow do not host radar-bright deposits, and that insolation was not the determining factor. Possible reasons for the lack of radar-bright deposits in such apparently conducive situations were mooted to be: a lack of radar coverage, unusually thick lag deposits hiding water ice from the radar, and an actual lack of water ice deposits.

These various lines of evidence collectively point to the presence of many reasonably pure water ice deposits in Mercury’s polar cold traps. Estimating the area covered by these deposits, either from radar measurements or maps of permanent shadow if the radar misses some (Deutsch et al. 2016), the remaining observational challenge in determining their volume is to measure their depth. While the neutron measurements suggest that the hydrogen-rich layer needs to be at least half a metre deep, for the radar results to arise due to volume scattering requires ice at least several wavelengths thick (Black et al. 2001; Harmon 2007). Given the results of Black et al. (2010) at 70 cm, this interpretation implies a layer of ice at least a few metres deep.

To place an upper limit on the thickness of possible water ice deposits in the Mercurian polar cold traps, a few different studies have considered the depth-diameter relations of craters. Barlow et al. (1999) anticipated that subsurface ice might lead to a softening of the terrain, as was seen on Mars (Cintala & Mouginis-Mark 1980; Squyres & Carr 1986). However, they found no unequivocal evidence of such an effect on Mercury’s craters, when split as a function of latitude. Vilas et al. (2005) extended this analysis, using the better resolution of the Harmon et al. (2001) radar results to focus on individual craters. With Mariner 10 imagery to determine crater depths and diameters, Vilas et al. (2005) found radar bright craters to have significantly lower depth-to-diameter ratios than radar dark ones, to an extent that could be explained by the presence of ~ 900 m of infilling material. Talpe et al. (2012) used the MLA data to study depth-to-diameter ratios in a sample of 537 craters poleward of 48°N . In contrast to Vilas et al. (2005), they found no evidence for different depths, slopes or surface roughnesses for radar-bright craters compared with their radar-dark counterparts. Ascribing the different results to having altimetry-derived measurements, Talpe et al. (2012) placed an upper limit on the depth of ice in a 10 km-diameter crater of ~ 300 m.

There are two orders of magnitude separating current lower and upper limits on the depth of the ice deposits in Mercury’s polar cold traps. This paper aims to determine how the existing MLA Gridded Data Record Digital Elevation Model (GDR DEM) can be used to improve the constraint on the depth of these deposits in craters near the north pole. The specific question being addressed is: are the radar-bright regions of polar crater interiors systematically elevated relative to otherwise similar radar-dark parts of the surface?

Section 2 describes the data being used in this study. The methods for constructing the crater sample and measuring the change in height associated with the radar-bright regions are detailed in both section 3 and appendix A. Section 4 contains the results of the analysis, and the implications are summarised in section 5.

2 DATA

This section contains descriptions of the topography and radar backscatter cross-section data sets used to study the Mercurian north polar craters. The topographical data were also used to define the crater populations within which the dependence of height with radar backscatter cross-section was studied.

2.1 Topographical data

Data from the 11th and 15th data releases (DR11 and DR15 hereafter) of the MLA GDR DEM, available from the Geosciences Node of NASA’s Planetary Data System (PDS¹), have been used. While DR11 contained a GDR at a spatial resolution of 500 m per pixel in a north polar stereographic projection, DR15 included both 250 m and 500 m resolution DEMs. All of these data sets were investigated in this study, to determine the best approach for constraining the thickness of Mercury’s polar deposits.

The MLA has absolute range uncertainties on individual altitude measurements of better than 1 m and an accuracy relative to the centre of mass of Mercury of better than 20 m (Sun & Neumann 2015; Zuber et al. 2012). Glitches are evident in the DR15 GDR, where the DEM height differs systematically along particular orbital tracks by of order ± 100 m relative to surrounding pixels. Thus, despite the improved sampling relative to the DR11 GDR, these glitches make the DR15 GDR unsuitable for this study and the DR11 500 m resolution option will be the default choice for the rest of this paper. A square region in the polar stereographic projection out to ± 1536 km from the north pole in both directions will be considered. This reaches a latitude $+55^\circ$ along the coordinate axes. The pixelated DEM has altitudes in the range $-6 < a/\text{km} < 2.5$, and the mean number of observations per pixel is ~ 0.11 . This sampling rate increases toward higher latitudes, peaking at ~ 0.5 observations per pixel at $+84^\circ$. The MLA GDR DEM includes interpolated altitudes for unobserved pixels.

2.2 Radar data

The Arecibo S-band (12.6 cm) radar data from Harmon et al. (2011)² were used to determine the radar properties of the surface in the vicinity of Mercury’s north pole; more specifically, the ~ 0.5 km pixelated same-sense circularly polarized cross-section map, σ_{SC} , shown in figure 4 of Harmon et al. (2011). These pixels slightly oversample the instrumental resolution of ~ 1.5 km, and there may be systematic location mismatches on the order of ~ 2 km between this radar grid and the MLA DEM (Harmon et al. 2011; Chabot et al. 2013; Deutsch et al. 2016). Root mean square measurement uncertainties on the individual pixel σ_{SC} values are ~ 0.014 and a threshold of 0.1 was adopted by default to separate radar-bright ($\sigma_{\text{SC}} > 0.1$) pixels from radar-dark ones. This is somewhat larger than the $4 \sigma_{\text{SC}}$ level advocated by Harmon et al. (2011), and should correspond to regions with thicker water ice deposits. Bilinear interpolation is used to associate a same-sense radar backscatter cross-section with each MLA pixel.

3 METHODS

This study requires an objectively selected set of craters and a method for assessing whether or not the radar-bright regions are typically at a different height to the radar-dark regions within the chosen craters. The construction of a crater catalogue from the

¹ <http://pds-geosciences.wustl.edu>

² available at <http://www.naic.edu/~radarusr/Mercpole/>

Table 1. Radii and locations for craters used in this study. Longitudes and latitudes are given in degrees. Crater numbers are shown in Fig. 1.

Crater #	Name	r_c /km	latitude, longitude
Radar-bright			
1	Yoshikawa	15.7	81.2, 106.0
2		13.6	82.7, 110.1
3	Laxness	12.3	83.3, -49.9
4	Ensor	12.6	82.3, -17.6
5	Carolan	12.4	83.9, 31.9
6	Desprez	23.2	81.1, -101.4
Radar-dark			
1	Fuller	13.3	82.6, -42.6
2	Varma	14.8	80.0, -18.8
3		14.9	83.6, -134.8
4		18.0	80.7, 142.9
5		17.1	82.9, -151.2
6		14.5	81.9, -152.3

DR11 MLA GDR DEM, the selection of craters from this catalogue, and the method of searching for height differences are described within the following three subsections.

3.1 Crater finding

To compare the heights of radar-bright and radar-dark regions within north polar craters requires a set of craters. As craters containing permanently shaded areas are quite deep, one would ideally have a set of such crater centres and their radii, co-registered with the MLA DEM in the vicinity of the north pole. Publicly available crater catalogues for Mercury exist, but are based on imagery, either from Mariner 10 and the early MESSENGER flybys that do not include much of one hemisphere near the north pole (Fassett et al. 2011; Herrick et al. 2011), or using the full MESSENGER set of images poleward of $+80^\circ$ (Deutsch et al. 2016).

Results from automated crater detection algorithms using only DEMs and not imagery have been reported in the past for crater finding on both the Moon (Luo et al. 2013; Xie et al. 2013; Li et al. 2015) and Mars (Bue & Stepinski 2007; Stepinski et al. 2009; Salamunicar & Loncaric 2010; Di et al. 2014), but not yet Mercury. As the focus of this paper is on deep, symmetric craters, a relatively simple crater detection algorithm has been designed that should recover such features from the MLA DEM.

The details of the algorithm being used here are given in the appendix. Briefly, the method involves filling up the DEM with virtual water and looking for near-circular depressions associated with the resulting puddles. When the depression stops being circular or having enough of a circular rim as the virtual water level increases, then a crater is defined by the final circle for which this depression was considered to be a crater candidate. A set of polar craters was found by applying this crater finding algorithm to a polar subset of the DR11 MLA GDR 500 m north pole stereographic DEM. This yielded 663 craters with radius, $r_c > 2$ km, of which 266 are poleward of $+80^\circ$. For comparison, the Deutsch et al. (2016) crater catalogue has 274 such craters. Most of the larger, fresher craters are in common between the MLA-based catalogue and that of Deutsch et al. (2016). However the image-based approach contains more craters with $r_c < 3$ km, where the MLA sampling makes it difficult to find circular depressions, and does not include some of the more degraded, larger craters that the MLA-based technique detects.

3.2 Crater selection

The craters to be considered need to be well-sampled by MLA pixels. They should also be large enough that mismatches between radar and topography data locations are small relative to the sizes of the craters. This puts limits on the range of latitudes and radii that are suitable. Craters with $80^\circ < \text{latitude} < 84^\circ$ and $r_c > 10$ km, with at least 15% of their 500 m pixels at $0.3 < r/r_c < 0.7$ containing DR11 observations are considered. Furthermore, younger craters should be more symmetric, having had less time for subsequent bombardment and morphological degradation. Using only younger craters will make it easier to see the signal of any ice-related non-axisymmetries in topography, without the additional noise caused by extensive sub-cratering. Therefore, craters with depth-to-diameter ratios of $d/D > 0.05$ are selected. Applying latitude, radius, MLA sampling and depth-to-diameter cuts leads to a sample of 12 craters.

The aim is to determine, for each crater of interest, whether the radar-bright pixels in the crater are higher or lower than the radar-dark ones at a similar crater-centric distance, r/r_c . In making this measurement, noise is introduced by both steep gradients within craters not being sampled in a similar fashion for radar-bright and radar-dark regions and subcratering. Two additional data cuts are applied to reduce the noise being introduced by these effects. Firstly, only pixels with $0.3 < r/r_c < 0.7$ are included in the analysis, removing regions with the steepest gradients caused either by central peaks or crater walls. Secondly, only pixels that were placed into each crater directly as the virtual water level rose are used, to remove any subcraters from the analysis. These extra cuts reduce the scatter in measured height differences between radar-bright and radar-dark regions that might otherwise act to obscure any small changes due to the presence of an ice deposit.

After pruning the data in this way, the remaining well-sampled craters are placed into either the radar-bright or radar-dark subset depending on the fraction of radar-bright MLA-sampled pixels, f , in the region $0.3 < r/r_c < 0.7$. A crater qualifies as radar-bright if $f > 0.1$, whereas radar-dark craters, which will be used as a control sample, have $f < 0.1$. These cuts lead to a sample of 6 radar-bright craters and 6 radar-dark ones. Figure 1 shows the whereabouts of the selected craters, along with some identifying numbers, and Table 1 lists their coordinates. The positions of these craters in the depth-diameter plane are shown in Figure A2. With the exception of Varma, which is very near to the $+80^\circ$ boundary, all of the craters in Table 1 are also present in the catalogue of Deutsch et al. (2016).

It should be noted that no assumption is made about the presence or otherwise of water ice in the radar-dark craters. Indeed, it is apparent in Figure 1 that two of the ‘‘radar-dark’’ sample have small regions where $\sigma_c > 0.1$. The presence of any significant ice deposits in these craters would make the control craters less axisymmetric. This, in turn, would broaden the distribution of height differences determined from the control sample. Hence, the confidence with which any height difference measured in the radar-bright sample could be ascribed to the presence of a volatile would be reduced. Thus the uncertainty derived from the control sample will be conservatively large as a result of any bias related to the possible presence of water ice in the control craters.

3.3 Measuring the height difference of the radar-bright regions

Given that craters are typically not perfectly axisymmetric and have complicated topographies as a result of subsequent impacts adding subcraters and degrading their rims, a statistical approach is adopted to determine if departures from axisymmetry in the crater topography correlate with the locations of radar-bright features.

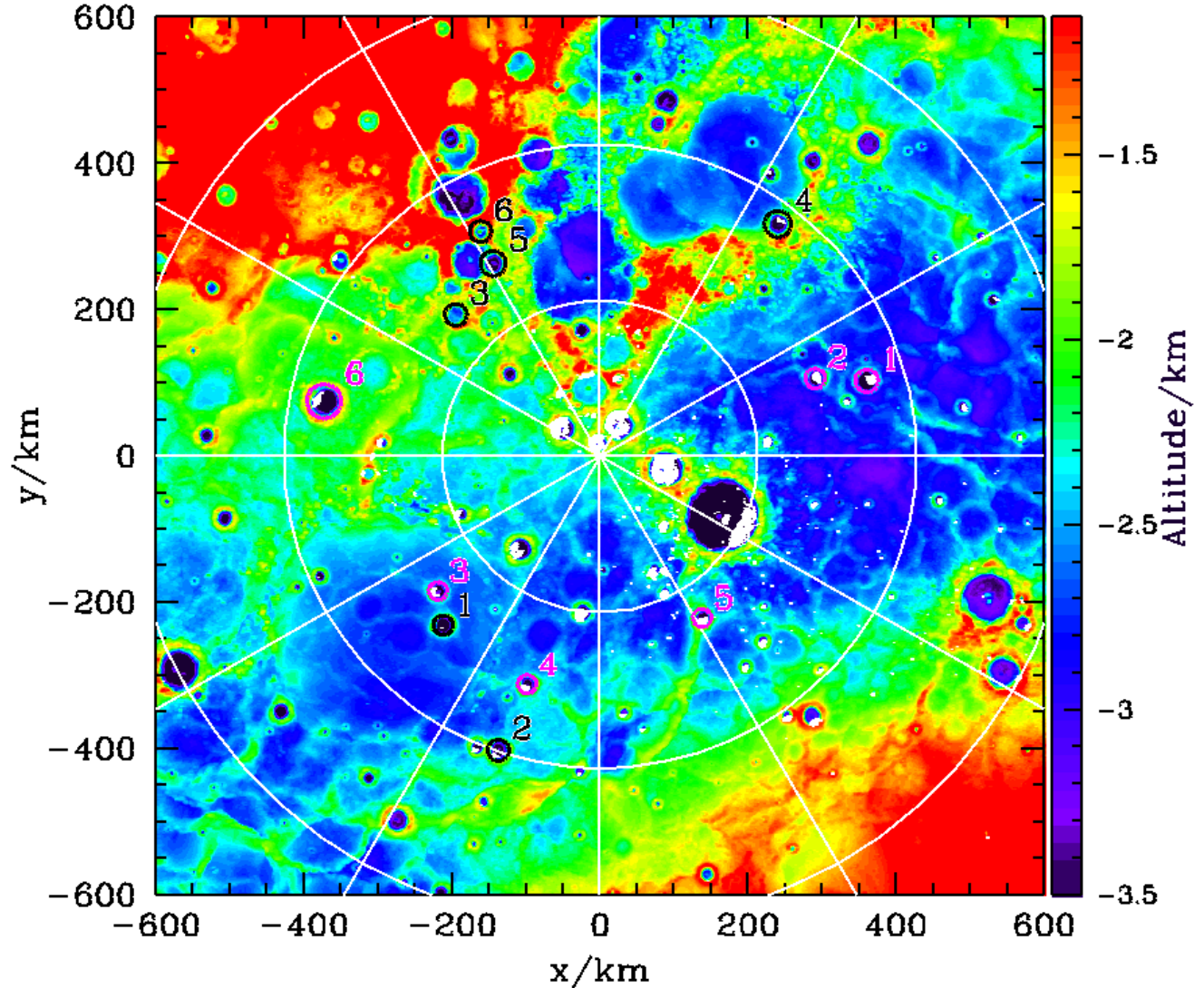


Figure 1. DR11 MLA GDR DEM, colour-coded by height. Magenta circles show the radar-bright crater sample, with their identifying numbers. Black circles are the control sample. White points show pixels where $\sigma_{sc} > 0.1$, according to the data of Harmon et al. (2011). White circles show latitudes of $+85^\circ$, $+80^\circ$ and $+75^\circ$, with white lines every 30° of longitude.

For each selected crater, the subset of observed pixels with $0.3 < r/r_c < 0.7$ that were placed into this crater directly were used. Pixels associated with puddles other than the one that gave rise to the crater being considered are excluded. The typical height as a function of cratercentric distance is determined empirically for each crater by ordering the remaining pixels in cratercentric distance and calculating the mean height of each consecutive set of 10 pixels. This number is chosen because smaller numbers of pixels produce very noisy results and larger numbers of pixels average over a wide range in surface height due to the non-flat shape of the crater. The results presented here are however robust to reasonable changes in this parameter choice.

Only pixels in the small radial ranges containing both radar-bright and radar-dark pixels are considered for further analysis. For each of these pixels, a height difference, Δh , is defined as the difference between its height and the mean height of the 10 pixels in its small radial range. Combining pixel Δh values from all relevant radial ranges in a crater, the median Δh values can be determined for the radar-bright and radar-dark subsets of the pixels. The differ-

ence between these values, $h_b - h_d$, defines the excess height of the radar-bright region relative to the radar-dark region in that crater. A height difference is measured for each crater, and the distribution of these height differences can be used to address the question: are the radar-bright regions of polar crater interiors systematically elevated relative to otherwise similar radar-dark parts of the surface?

4 RESULTS

Maps of pixel height difference, Δh , for each of the 12 craters being considered are shown in Figure 2, with the contour of high σ_{sc} superimposed for the 6 radar-bright cases. Within the craters, there are regional height deviations of typically ± 100 m from axisymmetry. The deviations from axisymmetry become largest at $r/r_c > 0.7$, on the steep parts of the crater walls. In some craters with central peaks, a similar effect can be seen at $r/r_c < 0.3$. The larger contiguous regions lacking Δh values are depressions other than that which gave rise to the main crater under consideration.

Figure 3 shows how pixel height difference, Δh , depends

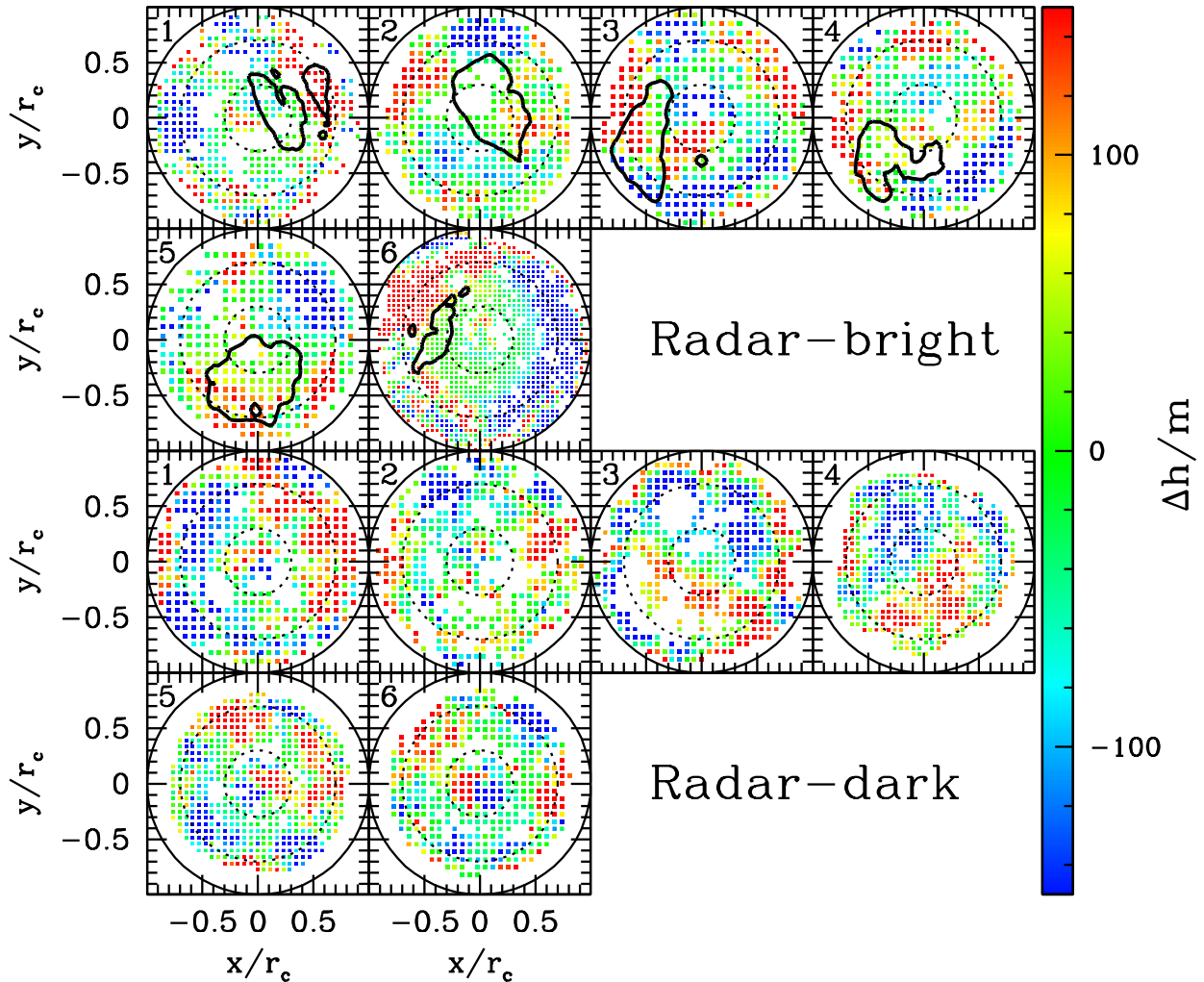


Figure 2. Maps of height difference, Δh , for the 6 radar-bright craters (top two rows), with crater 1 in the top-left panel. The radar-bright region ($\sigma_{sc} > 0.1$) is delineated with the thick black contour. A solid black circle shows the edge of the crater rim at $r/r_c = 1$, and dotted circles bound the region at $0.3 \leq r/r_c \leq 0.7$, from which the pixels are used for this analysis. The lower two rows contain the 6 radar-dark craters that form the control sample. In all cases, only pixels containing at least one observation and that were placed directly into the puddle that contained this crater are shown.

upon σ_{sc} for each of the radar-bright craters. The red points show the median pixel Δh values for the radar-bright and radar-dark pixels, and the difference between these two values defines the statistic $h_b - h_d$, which measures the excess height of the radar-bright region within each crater. For each of the six radar-bright craters under consideration, their radar-bright pixels are, in the median, systematically higher than the radar-dark ones. The distribution of the height difference, $h_b - h_d$, can be used to determine if this systematic difference is statistically significant.

For the control craters, the vast majority of pixels have $\sigma_{sc} < 0.1$. However, if the distributions of pixel Δh are compared for the radar-bright and radar-dark craters, then they are broadly similar, suggesting that the radar-dark craters provide a suitable control sample for estimating the statistical significance of the results. In order to define $h_b - h_d$ for the control sample of craters, the $\sigma_{sc} > 0.1$ regions in each of the 6 radar-bright craters are used as templates to define “radar-bright” regions in control craters. This should mean that any spatial correlations in Δh are treated similarly between the two crater samples. Thus, the control sample pro-

vides 6×6 ($h_b - h_d$) values. The cumulative distributions of the radar-bright and control crater height differences are shown in Figure 4, from which the median height difference for the radar-bright craters is 50 m.

A Kolmogorov-Smirnov (K-S) test says that, for a null hypothesis that all craters are drawn from the same population, there is a probability of 0.01 that these two distributions would be found. This is quite unlikely, in the direction that is supportive of the possibility that there are thick ice deposits associated with the radar-bright regions. However, the probability is artificially lowered by the fact that the control sample distribution has an upwards bump due to noise at $h_b - h_d \approx 40$ m, where the test statistic is being determined. The differential distribution of $h_b - h_d$ in the control crater sample is well described by a normal distribution with a standard deviation of 87 m, so a more robust assessment of the median excess height associated with the radar-bright regions in the six radar-bright craters would be (50 ± 35) m. This represents a detection of a non-zero deposit thickness at only a $\sim 1.5\sigma$ level of statistical significance.

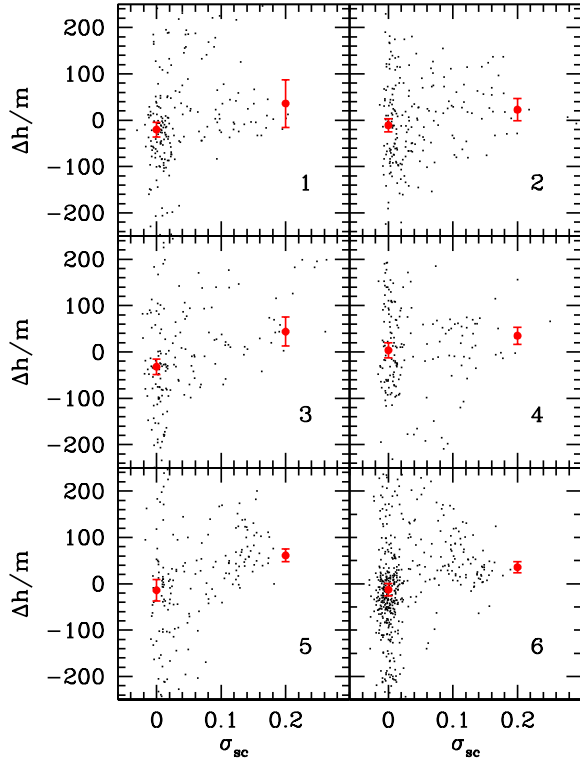


Figure 3. Dependence of pixel height difference, Δh , on same-sense radar backscatter cross-section for all pixels with $0.3 \leq r/r_c \leq 0.7$ within the six radar-bright craters. The crater number, as listed in Table 1, is shown in each panel. Red points show the medians of the radar-bright ($\sigma_{sc} > 0.1$) and radar-dark ($\sigma_{sc} < 0.1$) subsets of pixels. Error bars on the red points represent the 1σ errors on these medians, under the assumption that the individual pixel Δh values have a normal distribution.

If a threshold value of $\sigma_{sc} = 0.056$ had been chosen to differentiate between radar-dark and radar-bright regions, then Varma crater (number 2 in the radar-dark set) would switch to being a radar-bright crater, the K-S test would return a probability of ~ 0.09 and the median excess height would become (61 ± 44) m – again a $\sim 1.5\sigma$ detection. This illustrates how the K-S probability is less robust to small changes in the sample than the median height difference.

Also shown in Figure 4 is the cumulative height difference distribution for the control sample of 6 craters, where the “radar-bright” region has been chosen to be the pole-facing quadrant of the crater. No significant systematic height difference is apparent between the pole-facing part of these craters and the remaining 3 quadrants, with the median being ~ -10 m. Had these deep, polar, radar-dark craters contained very thick ($\gtrsim 100$ m) deposits on their pole-facing slopes, then this measurement should have detected them.

The craters in the radar-bright and control samples occupy similar regions in the crater depth-diameter diagram, as shown in Fig A2. There is no significant evidence of a correlation of height difference with any of crater depth, depth-to-diameter, number of observations or latitude. The results are robust to reasonable perturbations to the parameters of the crater-finding algorithm, because it tends always to find the same craters and the pixels that are excluded from the analysis are defined by the topography itself. Changing the selection of craters used to perform the test makes a larger difference to the results. By including smaller, less well-sampled craters, the significance of the difference between the

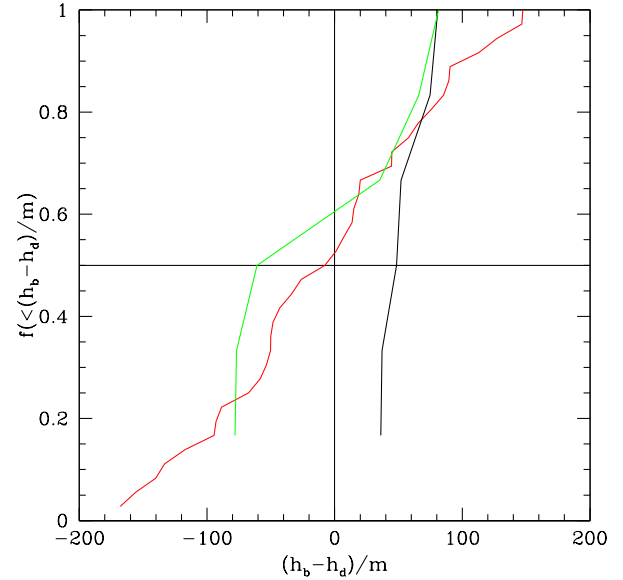


Figure 4. Cumulative distributions of the height difference between radar-bright and radar-dark pixels within the radar-bright (black) and control sample (red) craters. All 6 radar-bright craters have height differences in the range $36 < (h_b - h_d)/m < 81$, hence the steepness of the black curve. The red curve starts at a fraction of $1/36$, this being the number of different combinations of the 6 control craters and the 6 “radar-bright” region templates. A green curve traces the distribution of height differences for the control craters assuming that their “radar-bright” regions occupy the pole-facing quadrant of the craters.

radar-bright and control samples decreases. Similarly, extending the sample to lower or higher latitudes, where the craters are less well-sampled by MLA measurements also makes the distribution of height differences of the radar-bright sample look more like that of the control sample.

5 DISCUSSION

From this study, the typical excess thickness associated with the radar-bright regions in 6 north polar craters with diameters exceeding 20 km is (50 ± 35) m. While this does not represent a statistically significant measurement of a non-zero height increase in the radar-bright regions in polar cold traps, it does provide an upper limit of ~ 150 m on the depth of the typical ice deposit that may be associated with these regions. This is a factor of ~ 2 lower than that which was previously available (Talpe et al. 2012).

Given the typical, not ice-related, undulations in the surface within craters, it is not feasible to relate a localised change in height within any particular crater with the presence of a thick deposit of water ice. These departures from axisymmetry, even within fresh craters, can be up to ~ 100 m in amplitude. Consequently, improvements in range measurement accuracy, which is already much smaller than this, will not have a significant impact. More important would be both a more accurate positional matching between radar and DEM data sets, which would lead to reduced scatter in pixel Δh values caused by positional mismatches, and a denser sampling of the topography. These would permit a reliable extension of the technique developed here to include smaller craters containing radar-bright features. With a larger sample of craters, the difference between radar-bright and control craters could be more accurately determined. To some level, improved laser altimeter sampling is

provided by the MLA DR15 data although, as discussed earlier, there are presently some non-negligible glitches in the DR15 GDR that stymie this approach.

The BepiColombo Laser Altimeter (Thomas et al. 2007) is scheduled to map Mercury's surface in the next decade and will have a polar orbit with along-track resolution of ~ 250 m. At the end of the mission, the cross-track resolution should be better than ~ 1 km more than 80° from the equator. If the elliptical orbit sees BepiColombo flying low over the south pole, then this might double the number of available craters; otherwise, the anticipated lateral sampling will not differ greatly from that provided by the MLA.

Taken at face value, if a depth of 50 m of water ice were typical of all the radar-bright regions near the north pole of Mercury, then this would correspond to a total mass of water ice deposited near Mercury's poles of $\sim 10^{15}$ kg, assuming that the south pole contains a similar quantity, the water ice density is 10^3 kg m $^{-3}$ and using a value of $\sim 10,000$ km 2 for the total north pole radar-bright area (Harmon et al. 2011). If radar-dark permanently shaded regions also host deposits of water ice, then this value would represent an underestimate of the total mass present. Even so, this still amounts to more water ice than could feasibly be delivered to Mercury by micrometeorite bombardment, Halley-type comets or asteroids, according to the estimations of Moses et al. (1999). However, the value lies within their predicted range for water delivery from Jupiter-family comets. Given the uncertainty in the actual typical measured depth, it would be premature to rule out any of the alternative delivery sources on the basis of the results presented here. Furthermore, there are considerable uncertainties in the micrometeorite flux reaching Mercury, with recent studies by Borin et al. (2009); Nesvorný et al. (2010) and Bruck Syal et al. (2015) finding values that are respectively $\sim 60, 30$ and 10 times those assumed by Moses et al. (1999). However, this analysis does exclude the possibility of the total water ice deposits exceeding $\sim 3 \times 10^{15}$ kg, provided that the craters studied have ice depths typical of other regions hosting deposits.

ACKNOWLEDGMENTS

VRE acknowledges helpful discussions with Adrian Jenkins and Wenzhe Fa. VRE was supported by the STFC rolling grant ST/L00075X/1. This work used the DiRAC Data Centric system at Durham University, operated by the Institute for Computational Cosmology on behalf of the STFC DiRAC HPC Facility (www.dirac.ac.uk). This equipment was funded by BIS National E-infrastructure capital grant ST/K00042X/1, STFC capital grants ST/H008519/1 and ST/K00087X/1, STFC DiRAC Operations grant ST/K003267/1 and Durham University. DiRAC is part of the National E-Infrastructure.

REFERENCES

- Alexander C. M. O., Bowden R., Fogel M. L., Howard K. T., Herd C. D. K., Nittler L. R., 2012, *Science*, 337, 721
- Barlow N. G., Allen R. A., Vilas F., 1999, *Icarus*, 141, 194
- Black G. J., Campbell D. B., Harmon J. K., 2010, *Icarus*, 209, 224
- Black G. J., Campbell D. B., Nicholson P. D., 2001, *Icarus*, 151, 167
- Borin P., Cremonese G., Marzari F., Bruno M., Marchi S., 2009, *A&A*, 503, 259
- Bruck Syal M., Schultz P. H., Riner M. A., 2015, *Nature Geoscience*, 8, 352
- Bue B. D., Stepinski T. F., 2007, *IEEE Transactions on Geoscience and Remote Sensing*, 45, 265
- Butler B. J., 1997, *J. Geophys. Res.*, 102, 19283
- Butler B. J., Muhleman D. O., Slade M. A., 1993, *J. Geophys. Res.*, 98, 15
- Cavanaugh J. F., et al. 2007, *Space Sci. Rev.*, 131, 451
- Chabot N. L., Ernst C. M., Denevi B. W., Harmon J. K., Murchie S. L., Blewett D. T., Solomon S. C., Zhong E. D., 2012, *Geophys. Res. Lett.*, 39, L09204
- Chabot N. L., Ernst C. M., Denevi B. W., Nair H., Deutsch A. N., Blewett D. T., Murchie S. L., Neumann G. A., Mazarico E., Paige D. A., Harmon J. K., Head J. W., Solomon S. C., 2014, *Geology*, 42, 1051
- Chabot N. L., Ernst C. M., Harmon J. K., Murchie S. L., Solomon S. C., Blewett D. T., Denevi B. W., 2013, *Journal of Geophysical Research (Planets)*, 118, 26
- Cintala M. J., Mouginis-Mark P. J., 1980, *Geophys. Res. Lett.*, 7, 329
- Colaprete A., Schultz P., Heldmann J., Wooden D., Shirley M., Ennico K., Hermalyn B., Marshall W., Ricco A., Elphic R. C., Goldstein D., Summy D., Bart G. D., Asphaug E., Korycansky D., Landis D., Sollitt L., 2010, *Science*, 330, 463
- Crater Analysis Techniques Working Group 1979, *Icarus*, 37, 467
- Crider D., Killen R. M., 2005, *Geophys. Res. Lett.*, 32, L12201
- Davis M., Efstathiou G., Frenk C. S., White S. D. M., 1985, *ApJ*, 292, 371
- Deutsch A. N., Chabot N. L., Mazarico E., Ernst C. M., Head J. W., Neumann G. A., Solomon S. C., 2016, *Icarus*, 280, 158
- Di K., Li W., Yue Z., Sun Y., Liu Y., 2014, *Advances in Space Research*, 54, 2419
- Eke V. R., Bower K. E., Diserens S., Ryder M., Yeomans P. E. L., Teodoro L. F. A., Elphic R. C., Feldman W. C., Hermalyn B., Lavelle C. M., Lawrence D. J., 2015, *Journal of Geophysical Research (Planets)*, 120, 1377
- Fassett C. I., Kadish S. J., Head J. W., Solomon S. C., Strom R. G., 2011, *Geophys. Res. Lett.*, 38, L10202
- Hagfors T., Dahlstrøm I., Gold T., Hamran S.-E., Hansen R., 1997, *Icarus*, 130, 313
- Hapke B., 1990, *Icarus*, 88, 407
- Harmon J. K., 2007, *Space Sci. Rev.*, 132, 307
- Harmon J. K., Perillat P. J., Slade M. A., 2001, *Icarus*, 149, 1
- Harmon J. K., Slade M. A., 1992, *Science*, 258, 640
- Harmon J. K., Slade M. A., Rice M. S., 2011, *Icarus*, 211, 37
- Harmon J. K., Slade M. A., Vélez R. A., Crespo A., Dryer M. J., Johnson J. M., 1994, *Nature*, 369, 213
- Hartogh P., Lis D. C., Bockelée-Morvan D., de Val-Borro M., Biver N., Küppers M., Emprechtinger M., Bergin E. A., Crovisier J., Rengel M., Moreno R., Szutowicz S., Blake G. A., 2011, *Nature*, 478, 218
- Herrick R. R., Curran L. L., Baer A. T., 2011, *Icarus*, 215, 452
- Ingersoll A. P., Svitek T., Murray B. C., 1992, *Icarus*, 100, 40
- Lawrence D. J., Feldman W. C., Goldsten J. O., Maurice S., Pelpowski P. N., Anderson B. J., Bazell D., McNutt R. L., Nittler L. R., Prettyman T. H., Rodgers D. J., Solomon S. C., Weider S. Z., 2013, *Science*, 339, 292
- Li B., Ling Z., Zhang J., Wu Z., 2015, *Earth Moon and Planets*, 115, 59
- Luo L., Mu L., Wang X., Li C., Ji W., Zhao J., Cai H., 2013, *Frontiers of Earth Science*, 7, 456
- Morbidelli A., Chambers J., Lunine J. I., Petit J. M., Robert F., Valsecchi G. B., Cyr K. E., 2000, *Meteoritics and Planetary Science*, 35, 1309
- Morbidelli A., Lunine J. I., O'Brien D. P., Raymond S. N., Walsh K. J., 2012, *Annual Review of Earth and Planetary Sciences*, 40, 251
- Moses J. I., Rawlins K., Zahnle K., Dones L., 1999, *Icarus*, 137, 197
- Nesvorný D., Jenniskens P., Levison H. F., Bottke W. F., Vokrouh-

- lický D., Gounelle M., 2010, *ApJ*, 713, 816
- Neumann G. A., Cavanaugh J. F., Sun X., Mazarico E. M., Smith D. E., Zuber M. T., Mao D., Paige D. A., Solomon S. C., Ernst C. M., Barnouin O. S., 2013, *Science*, 339, 296
- O'Brien D. P., Walsh K. J., Morbidelli A., Raymond S. N., Mandell A. M., 2014, *Icarus*, 239, 74
- Ong L., Asphaug E. I., Korycansky D., Coker R. F., 2010, *Icarus*, 207, 578
- Paige D. A., Siegler M. A., Harmon J. K., Neumann G. A., Mazarico E. M., Smith D. E., Zuber M. T., Harju E., Delitsky M. L., Solomon S. C., 2013, *Science*, 339, 300
- Paige D. A., Wood S. E., Vasavada A. R., 1992, *Science*, 258, 643
- Pike R. J., 1988, *Geomorphology of impact craters on Mercury*, pp 165–273
- Salamuniccar G., Loncaric S., 2010, *IEEE Transactions on Geoscience and Remote Sensing*, 48, 2317
- Slade M. A., Butler B. J., Muhleman D. O., 1992, *Science*, 258, 635
- Solomon S. C., McNutt R. L., Gold R. E., Domingue D. L., 2007, *Space Sci. Rev.*, 131, 3
- Sprague A. L., Hunten D. M., Lodders K., 1995, *Icarus*, 118, 211
- Squyres S. W., Carr M. H., 1986, *Science*, 231, 249
- Stepinski T. F., Mendenhall M. P., Bue B. D., 2009, *Icarus*, 203, 77
- Stewart B. D., Pierazzo E., Goldstein D. B., Varghese P. L., Trafton L. M., 2011, *Icarus*, 215, 1
- Sun X., Neumann G. A., 2015, *IEEE Transactions on Geoscience and Remote Sensing*, 53, 2860
- Talpe M. J., Zuber M. T., Yang D., Neumann G. A., Solomon S. C., Mazarico E., Vilas F., 2012, *Journal of Geophysical Research (Planets)*, 117, E00L13
- Thomas N., et al. 2007, *P&SS*, 55, 1398
- Vasavada A. R., Paige D. A., Wood S. E., 1999, *Icarus*, 141, 179
- Vilas F., Cobian P. S., Barlow N. G., Lederer S. M., 2005, *P&SS*, 53, 1496
- Xie Y., Tang G., Yan S., Lin H., 2013, *IEEE Geoscience and Remote Sensing Letters*, 10, 885
- Zuber M. T., et al. 2012, *Science*, 336, 217

APPENDIX A: CRATER-FINDING ALGORITHM

In designing an automated crater-finding algorithm, the main challenges arise because craters become degraded and often overlap with one another. The algorithm needs to allow for the possibilities that some craters can lie entirely within other craters, and that some may only retain a small fraction of a circular rim. The approach taken here is motivated by the expectations that craters will include a local minimum in the topography, which is not inevitably the case but should be true in the vast majority of cases, and have at least some part of a near-circular edge.

The crater-finding algorithm comprises two main stages, the first of which involves gradually filling up the DEM with virtual water and creating a tree-like structure of interconnected puddles. The second stage searches through the sets of resulting puddles looking for near-circular depressions. It will be assumed that any near-circular depression is a crater, although this need not be the case. These two operations are described in this appendix.

A1 Creating the puddle tree

A set of virtual water levels spaced by $\delta a = 1$ m were used gradually to fill up the terrain. At first a single, pixel-sized puddle was present. Subsequently other puddles appeared and merged together until a single large puddle covered the entire domain.

For each water level, a two-dimensional friends-of-friends algorithm (Davis et al. 1985) was run to find distinct puddles. This involves linking together wet pixels, i.e. those at altitudes beneath the virtual water level, with their wet neighbours, including diagonal links. If two or more puddles at one level are linked together at the next, when the water level increases by δa and creates more wet pixels, then the smaller progenitor puddles are noted as having merged into the larger/largest progenitor, which retains its identity. In this way a tree-like structure of puddles is built up. This tree can be traversed in order to track the varying shape of any puddle as the water level is increased.

Applying this friends-of-friends algorithm to the 500 m MLA GDR DEM north polar stereographic projection from DR11 leads to the identification of 362248 distinct puddles. These puddles are present for at least one of the 8453 virtual water levels. Had the number of levels been halved by choosing $\delta a = 2$ m, then the number of distinct puddles would have decreased only slightly to 344245.

A2 Finding near-circular depressions using the puddle tree

Each puddle that appears as the virtual water level increases can give rise to many craters. It is also possible that it will not host any craters. The second part of the crater-finding algorithm involves finding near-circular puddles, tracking how these crater candidates evolve as the virtual water level rises, and logging them as craters at the level before they cease to have a sufficiently detectable near-circular edge. This subsection defines what it means to be near-circular and how the crater candidates are treated if their host puddles merge into other puddles.

At a given virtual water level, a puddle is defined as a set of pixels. Puddles are split into “main” puddles, which have yet to merge into a larger pre-existing puddle as the virtual water level rises, and “progenitor” puddles, which have already merged into a larger puddle. The 500 m sampling of the DEM limits the ability to determine how circular small puddles are, so only puddles containing an area of wet pixels $A \geq \pi r_{c,\min}^2$ are considered as potential hosts of crater candidates. For the results presented here, the choice $r_{c,\min} = 2$ km has been used, for which the diameter of the crater will be sampled with 8 pixels. Smaller puddles are too poorly sampled to determine if they are sufficiently circular. At every virtual water level, every main puddle present is assessed to determine if it contains a crater candidate. All crater candidates from progenitor puddles are also tracked to determine if they remain crater candidates. The centres and radii of crater candidates are updated.

There are three distinct methods used to determine if a crater candidate exists or remains in each sufficiently big main puddle, the second and third of which are used for crater candidates in progenitor puddles.

1) For main puddles only, all pixels are used to determine $I = \pi \langle r^2 \rangle / A$, where $\langle r^2 \rangle$ represents the mean-squared separation of the constituent pixels from their mean location. If $I < I_{\max}$ then this puddle is sufficiently circular to be a viable crater candidate. Small fluctuations of I near to I_{\max} can lead to multiple detections of what is essentially the same crater. To suppress the frequency of such events, any crater candidate at the previous, lower level, remains viable provided that $I < I_{\max} + \delta I$. For this work, $I_{\max} = 0.53$ and $\delta I = 0.02$. The candidate crater centre and radius, defined as $r_c = \sqrt{A/\pi}$, are updated at each level. Also, if a main puddle will become a progenitor puddle at the next level and is not a crater candidate, then its centre and “radius” are stored.

If method (1) has failed to find a crater candidate for a sufficiently big main puddle, or a crater candidate in a progenitor puddle is being tracked from the previous level, then the following procedure is followed to hunt for a crater candidate.

2) The set of dry perimeter pixels around the main puddle are found, not including diagonal steps. Near-circular arc is defined as the total area, A_{per} of perimeter pixels whose centres lie in the range $[r_c - \delta r/2, r_c + \delta r/2]$ from the crater candidate centre found at the previous level, where $\delta r = 1.0$ km is used here. If $A_{\text{per}} > f_{\text{rim}} 2\pi r_c \delta r$, where $f_{\text{rim}} = 0.4$, then a potential crater candidate exists. For just-merged progenitor puddles that contained no crater candidate at the final level when they were main puddles, the near-circular arc pixels are allowed to lie in the range $[0, \max(2r_c, r_c + 5\delta r/2)]$.

If this method finds sufficient near-circular arc, then the potential crater candidate centre and radius are determined using the perimeter pixels that comprise the near-circular arc. This is done by taking up to 10^6 distinct tuples of these pixels and determining the centres and radii of the circles they define. The centres that lie within a distance $2f_{\text{shift}}r_c$ of the previous centre, where $f_{\text{shift}} = 0.1$, are retained and a shrinking circles algorithm is applied to determine the potential crater candidate centre. This involves iteratively calculating the mean position of the remaining centres then reducing the radius within which centres are included by 5% before repeating. When no more than 30 centres remain, their mean position is returned as the centre of the potential crater candidate. The radius is taken to be the median of the radii associated with the remaining centres. If the centre of the potential crater candidate lies within a distance $f_{\text{shift}}r_c$ of the previously calculated centre, and the radius is no more than 10% larger than the previously calculated radius, then this potential crater candidate is deemed to be a crater candidate. Otherwise, assuming that a crater candidate did exist at the preceding virtual water level, one final method is attempted to try to locate a viable crater candidate.

3) It is possible that the perimeter of dry pixels around a puddle in the vicinity of a crater candidate does not enclose its centre. For example, if the crater rim is irregular in height and only a subset locally pokes above the virtual water level. In this case, rather than using the puddle perimeter as was done in method (2), potential dry rim pixels are sought a distance $[r_c - \delta r/2, r_c + \delta r/2]$ away from the previous crater candidate centre. If the area of dry rim satisfies $A_{\text{rim}} > f_{\text{rim}} 2\pi r_c \delta r$, then a viable crater candidate remains and its radius is updated to be the mean radius of the dry rim pixels from the previous centre. The centre is not updated in this method.

If a crater candidate existed at the previous level and it ceases to exist, then its last acceptable centre and radius are logged as a crater.

A3 Results

Applying the algorithm described above to the MLA GDR DR11 leads to a database of 663 craters with radii ≥ 2 km. The crater counts as a function of crater diameter are shown in Fig. A1, in comparison with the results from Fassett et al. (2011) and Herrick et al. (2011). It is important to note that the catalogues provided by Fassett et al. (2011) and Herrick et al. (2011) are derived from MESSENGER and Mariner 10 images that only adequately cover approximately half of the area being used. As a consequence, the abundances shown in Fig. A1 have been multiplied by 2 to account for this survey mask. This factor of two is approximately the incompleteness in the catalogue derived here for crater sizes in the range $10 \lesssim r_c/\text{km} \lesssim 25$. The incompleteness is greater for larger craters. This reflects the difficulty of automatically finding very degraded craters. However, the new set of craters extends down to smaller radii than were previously available, and covers the entire range of longitudes near to the north pole.

The various different lines in Fig. A1 show the effect of using data from different releases (DR11 and DR15), with different pixel sizes (250 m and 500 m) and using different values for the

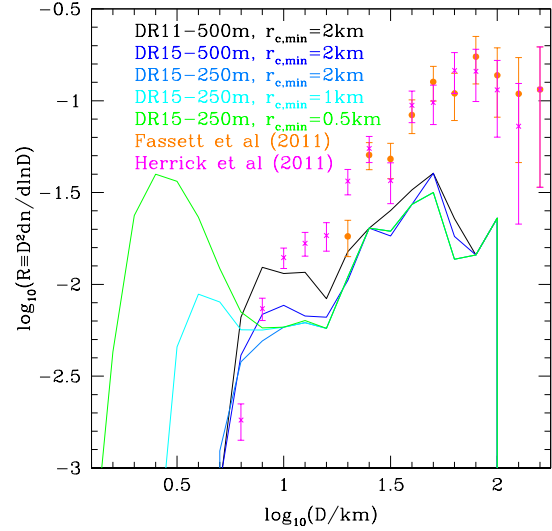


Figure A1. The abundance of craters as a function of crater diameter, D for the region $|x|, |y| < 800$ km from the pole in the polar stereographic projection. The standard R -plot is shown (Crater Analysis Techniques Working Group 1979), where n represents the number of craters per unit area. Curves represent the crater abundances from applying the algorithm described in this appendix to the different GDR data releases, at different pixel resolutions, with different minimum crater candidate sizes, as shown in the legend. The points with error bars are using craters from the catalogues of Fassett et al. (2011) and Herrick et al. (2011) in the same region.

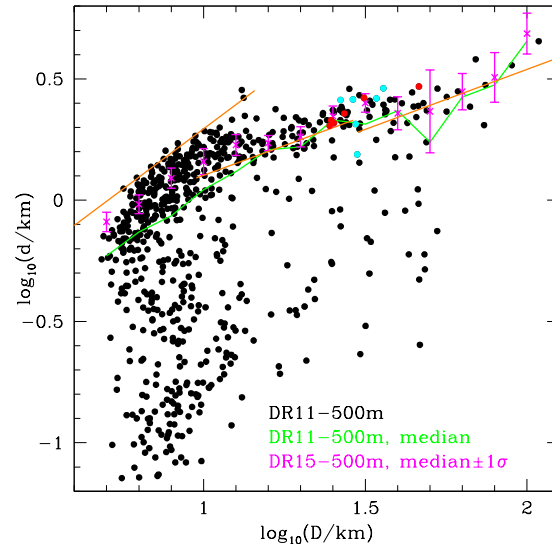


Figure A2. The depth-diameter relation for the recovered craters. Black filled circles show all 663 DR11 craters found using $r_{c,\text{min}} = 2$ km, and the green line traces the median depth as a function of diameter. The magenta crosses are the corresponding medians for the 663 DR11 craters, with error bars showing the errors on the median depths under the assumption of Gaussian distributed depths at each diameter. In order of increasing diameter, the three orange lines represent the relations for simple craters, immature and mature complex craters determined by Pike (1988). Red and cyan filled circles show the 6 radar-bright and 6 radar-dark craters respectively used in this study.

parameter $r_{c,\min}$. The difference between green and cyan curves is that crater candidates are allowed to be smaller in the former case. Given that these $r_{c,\min}$ values are close to the pixel size in the DEM, it is difficult to determine accurately whether or not a puddle is nearly circular enough to host a crater candidate. From the convergence of the curves, it appears that the results are robust for craters with $r_c \geq 3$ km, which is approximately 10 times the pixel size. The blue curve shows how using the 500 m-resolution DEM, rather than the 250 m DEM alters the crater abundances. A more significant change is seen when using the DR11 GDR. Almost twice as many $r_c \sim 10$ km craters are found. The results converge for larger craters. While the DR11 GDR is less well-sampled than DR15, the newer release contains glitches, where particular orbits are $\sim \pm 100$ m different in height than the surrounding measurements, so it is not immediately clear which of these data sets is to be preferred.

Another interesting way to characterise the craters is through their depth and diameter. These are shown in Fig. A2, where the crater depth is simply defined as the height difference between the minimum and maximum altitude pixels with centres lying within r_c of the crater centre. The set of DR11 craters includes significantly more shallow, small-diameter craters than for the DR15 case, pulling the median depth down for this case. In comparison with the results of Pike (1988), the automatically found craters are typically slightly shallower than his simple crater sample and deeper than his complex craters. Given the different methods for finding craters and measuring diameters and depths, the results are similar.

In summary, the automated DEM-based crater-finding algorithm presented here is finding approximately half the larger craters present in the Fassett et al. (2011) and Herrick et al. (2011) samples, as well as plenty of smaller ones. The missing craters are predominantly those that are less well-defined due to degradation by subsequent bombardment. For the purpose of the study presented here, the fact that the algorithm is finding the deep, fresh craters is the most important point.